Fault Modeling of Implantable MEMS Sensors

J. A. Miguel[1], Y. Lechuga[1], M. Martinez[1] and J. R. Berrazueta[2]

[1]*Microelectronics Group, TEISA Department, University of Cantabria, Avda de los Castros s/n, Santander, Spain*
[2]*Department of Medicine, Faculty of Medicine, University of Cantabria, Avda de Valdecilla s/n, Santander, Spain*

Keywords: MEMS Testing, Fault Injection, Biomedical Transducers, Implantable Biomedical Devices, Cardiology.

Abstract: The aim of this work is to analyse the fault-injection problem of implantable capacitive micro-electro-mechanical pressure sensors intended to be used as a part of smart stents for in-stent restenosis monitoring. The development of accurate fault models is mandatory in order to create a Design-for-Test methodology compatible with MEMS-based sensors as well as with its related CMOS electronic circuitry. Rigorous behavioural descriptions of both circular and square-shaped fault-free pressure sensors can be obtained from analytical expressions and numerical approximations. However, the deflection vs. pressure response of faulty sensors, suffering from contamination-based defects growth during the fabrication process, require the use of finite-elements analysis to be modelled, allowing the fulfilment of a realistic fault model library.

1 INTRODUCTION

During the last decade, the fast development of Micro-Electro-Mechanical Systems (MEMS), in conjunction with the build-up of new fabrication technologies compatible with CMOS processes has made possible the production of heterogeneous systems, integrating MEMS structures and electronic circuits on the same silicon substrate. In this way, a miniaturization of implantable electronic devices has been achieved, increasing their capabilities and uses.

Nowadays, Atherosclerosis, affecting cardiac, cerebral, renal or peripheral vascular vessels, is the most prevalent disease in developed countries, responsible for nearly 47% of deaths in Europe. The related treatment costs reach about 9% of the total healthcare expenditure from countries across the EU, with inpatient hospital care comprising 49% of these costs (Nichols et al., 2012).

Percutaneous Coronary Interventions (PCI), allow an accurate diagnosis of obstructive lesions using arteriography, as well as a reliable treatment through balloon angioplasty, generally accompanied by stenting. In Spain, nearly 124.000 diagnostic coronary angiograms are performed annually. In 66.000 of these cases an angioplasty is performed, and in 55.000 cases 100.000 stents are implanted, trying to avoid restenosis, the most important sequela of this technique (Garcia B. et al., 2013).

Severe and symptomatic carotid lesions have a similar treatment by neuroradiologists. In general population, total severe carotid stenosis is estimated in less than 1%. However the prevalence of lesions greater than 50% in population younger than 70 years is 4.8% in men and 2.2% in women, rising to 12.5% for males and 6.9% for women over 70 years (Wolff T. et al., 2007).

The prevalence of lower extremity Peripheral Artery Disease (PAD) ranges from 3% to 12%, with 202 million people affected in 2010 (Fowkes F.G. et al., 2013). The annual incidence of critical ischemia of the lower extremities varies from 500 to 1.000 new cases per million population, being higher for patients with diabetes (Tendera M. et al., 2011).

During angioplasty, a flexible balloon catheter is threaded into the blockage location and inflated, applying a controlled pressure which compresses the plaque deposition against the artery walls. Angioplasty is usually accompanied by stents placed surrounding the tip of the balloon catheter. Once the balloon tip is inflated, the stent spring is opened and attached to the vessel walls, remaining in place after the balloon is deflated and removed. Thus, the stent holds the vessel open, lessening the risk of re-narrowing due to elastic recoils and spasms. However, In-Stent Restenosis (ISR), a process of neointimal tissue growth inside the stent, supposes a major drawback to angioplasty reliability.

ISR monitoring is carried out nowadays using expensive techniques, like angiography and intravascular ultrasound. Smart stents, implantable electronic devices able to sense and transmit real-

time data from physiological signals related to the vessel condition, have positioned themselves as an economic alternative to ISR follow-up.

Smart stents, as implantable electronic devices, must fulfil certain design constraints, including small size, low power requirements, output stability, and reliability over time without recalibration. This last challenge makes testing and fault modelling critical issues to validate the fabricated device.

Generally, MEMS testing has been limited to a set of electrical, optical and mechanical analyses, used to check the functionality of the device. However, the correlations between the detected failures and their underlying physical causes are usually missing. These relationships are needed to allow an accurate modelling of complex fabrication defects, and can be useful in the generation of realistic faults models, as well as in the development of capable testing techniques. For this reason, fault models must include real defective behaviours in order to reach high fault coverage and test quality.

This work focuses on the generation of a fault model for an implantable MEMS capacitive pressure sensor. Finite Elements (FE) tools have been proven to be necessary to model those faults whose complexity makes analytical descriptions inapt. The results from FE analysis will give rise to a realistic fault model library, and to the development of a comprehensive Design-for-Test (DfT) methodology.

In Section 2, the most common failure mechanisms affecting MEMS devices are described. Section 3 introduces the proposed heterogeneous system, focusing on the analytical modelling of its MEMS sensors under fault-free conditions. Section 4 illustrates the need of FE analysis to model the behaviour of MEMS sensors under the presence of certain faults. Finally, in Section 5 conclusions are presented.

2 MEMS FAULT CLASSES AND FAILURE MECHANISMS

Several failure mechanisms or defects can appear during the fabrication process of heterogeneous devices, being possible to distinguish between defects arising during the CMOS process and defects occurring during micromachining.

Microelectronic and MEMS components can be created on the same silicon substrate by means of a set of conductor, semiconductor and dielectric layers. Each one of the technological operations used to grow these layers, such as oxidation,

deposition, photolithography or etching, is a potential source of defects, where contaminants can appear, degrading the succeeding fabrication steps.

In the particular case of CMOS-compatible MEMS, failure mechanisms can be classified according to the physical property being affected. MEMS faults can be initially grouped into parametric or catastrophic types, in the same way as for analog testing. However, the nature of MEMS devices gives rise to new types of manufacturing defects, which require an extended classification scheme. Thus, it is necessary to distinguish between faults affecting the microsystem gauge and those affecting the supporting structure. Each of these faults can be again classified as a parametric fault, changing the physical properties of the device and altering its performance; or as a catastrophic fault, preventing any use of the system.

In this work, the case of impurities appearing during the anisotropic wet etching process used to create diaphragms is analysed in detail. Impurities in the form of small crystal lattice defects located in the bulk material during this process can cause the growth of pyramids on top of the diaphragm. Depending on their size and location, these pyramids can strongly change the properties of the diaphragm. As can be seen in Fig. 1, the sidewall slope of the pyramids is a fixed parameter which depends on the angles between the main crystal planes of a single silicon crystal. For instance, this slope presents a value of 54.7° in the case of anisotropic wet etching of a {100} oriented wafer, corresponding to the angle between the {100} and {111} planes. It must be noticed that the height of the pyramid can be obtained from the sidewall slope, so a change in the base length of the pyramid will alter its size (Rosing, Reichenbach, Richardson, 2002) (Landsberger, Nashed, Kahrizi, Paranjape, 1996).
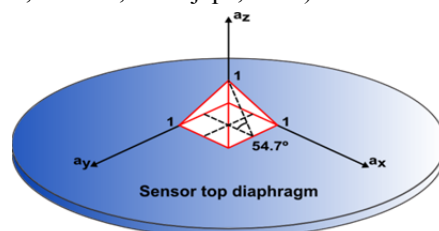

Figure 1: Pyramid defect growth during anisotropic wet etching process.

3 MEMS PRESSURE SENSOR MODELLING

One of the simplest and more reliable smart stent

designs for ISR monitoring is made up of two MEMS capacitive pressure sensors attached at opposite sides of a regular stent. In this way, the pressure gradient along the device (implanted in a distal pulmonary artery) can be measured and wirelessly transmitted outside the patient body by means of an LC tank formed by the sensors and the body of the stent (Takahata, Gianchandani, Wise, 2006).

The proposed MEMS capacitive pressure sensor to be included in the above-mentioned smart stent can be split into two different parts: a fully-clamped suspended flexible top diaphragm anchored to the substrate, and a fixed back plate. The principle of operation governing the behaviour of this kind of sensors is based on the concept of a two parallel plate capacitor, where the resultant capacitance is inversely proportional to the distance between the plates.

Fig. 2 shows a simplified cross-sectional view of a MEMS capacitive pressure sensor with an air-filled cavity. When a certain pressure P is uniformly applied to the top plate, with a thickness t_m, a deflection is induced, reducing the initial gap t_g between the plates and increasing the sensor capacitance. The parameter w_0 refers to the maximum deflection of the plate.
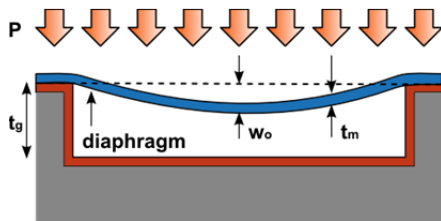

Figure 2: Cross-sectional view of a MEMS capacitive pressure sensor.

The equivalent capacitance of a MEMS pressure sensor can be analytically calculated by the expression stated in (1), where C_0 is the capacitance of the undeformed sensor, ε_0 is the dielectric permittivity of the void, and A is the overlapped area between both plates.

$$\Delta C = C_S - C_0 = \iint_A \frac{\varepsilon_0 \cdot dx \cdot dy}{t_g - w(x,y)} - \varepsilon_0 \frac{A}{t_g} \qquad (1)$$

3.1 Circular Sensor

An analytical behavioural modelling of a fully-clamped diaphragm can be achieved only when certain conditions are fulfilled: (a) the fabrication material of the top diaphragm must have isotropic

mechanical properties; (b) the thickness of the metallic electrode on the top plate is required to be smaller than the thickness of the plate in order to be neglected; (c) the initial gap between the plates must be small compared to the lateral extents of the plates, so that the influence of the field fringing effects could be neglected; (d) the residual stresses in the flexible diaphragm are not considered. Once all the requirements have been met, the plate deflection at radius r, of a fully clamped circular diaphragm, can be expressed as:

$$w(r) = w_0 \left[1 - \left(\frac{r}{a} \right)^2 \right]^2 \qquad (2)$$

Where r is the distance of the point of interest to the centre of the diaphragm, a is the radius of the diaphragm and w_0 is the maximum centre deflection.

Depending on the sensor deflection-to-thickness ratio, the maximum centre displacement can be analytically modelled using different expressions, as described in (Timoshenko, Woinowsky-Krieger, 1959). The centre displacement vs. pressure relationship for both small and large deflection conditions can be approximated as (Timoshenko, Woinowsky-Krieger, 1959):

$$w_0 = \frac{3 \cdot P \cdot a^4 \cdot (1 - v^2)}{16 \cdot E \cdot t_m^3} \cdot \frac{1}{1 + \frac{0.488 \cdot w_0^2}{t_m^2}} \qquad (3)$$

Where P is the pressure applied to the diaphragm, a is its radius, and υ and E are the Poisson's ratio and Young's modulus of elasticity of the diaphragm material respectively.

3.2 Rectangular Sensor

The deflection of a rectangular flexible diaphragm, as shown in Fig. 3, can be analytically modelled by a set of differential equations (4) and (5). Some conditions have to be fulfilled to validate the model: (a) the diaphragm must be fully clamped at its edges; (b) the bending of the diaphragm must be elastic; (c) the deflection has to remain smaller than half the thickness of the diaphragm.
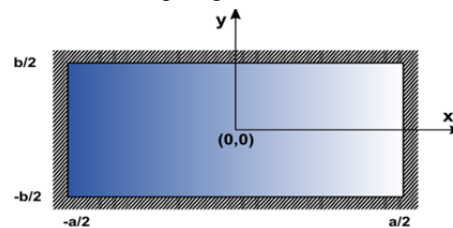

Figure 3: Coordinate system of a rectangular diaphragm.

Thus, the fully clamped rectangular diaphragm deflection vs. pressure relationship can be approximated by the following differential equation and its boundary conditions:

$$\frac{\partial^4 w}{\partial x^4} + 2 \cdot \alpha \cdot \frac{\partial^4 w}{\partial x^2 \partial y^4} + \frac{\partial^4 w}{\partial y^4} = \frac{P}{D_0 \cdot t_m^3} \qquad (4)$$

$$w\left(x = \pm \frac{a}{2}; y\right) = 0$$

$$w\left(x; y = \pm \frac{b}{2}\right) = 0$$

$$\frac{\partial w}{\partial x}\left(x = \pm \frac{a}{2}; y\right) = 0 \qquad (5)$$

$$\frac{\partial w}{\partial x}\left(x; y = \pm \frac{b}{2}\right) = 0$$

Where

$$\alpha = \upsilon + \frac{2 \cdot E_t \cdot (1 - \upsilon^2)}{E} \qquad (6)$$

$$D_0 = \frac{E}{12 \cdot (1 - \upsilon^2)} \qquad (7)$$

and a, b, E, E_t and υ are the diaphragm x-length and y-length, the Young's elasticity modulus, the shear modulus and Poisson's ratio, respectively.

The following changes in variable are introduced to limit the integration domain to a square of unit side:

$$X = \frac{2x}{a}; -1 \le X \le 1$$
$$Y = \frac{2y}{b}; -1 \le Y \le 1 \qquad (8)$$

The system of differential equations can be approximated via several mathematical methods. The Galerkin method has been applied (Timoshenko, Woinowsky-Krieger, 1959), leading to the following analytical result:

$$w(x, y, P) = w_0 \cdot f(X, Y, r) \qquad (9)$$

$$w_0 = \frac{k(r) \cdot a^2 \cdot b^2}{16 \cdot D_0 \cdot t_m^3} \cdot P \qquad (10)$$

$$f(X, Y, r) =$$
$$\left[(1 - X^2)(1 - Y^2)\right]^2 \sum_{i=0}^{n} \sum_{j=0}^{n} k_{ij}(r) X^i Y^j \qquad (11)$$

Where n is an even positive integer; i, j=0, 2, 4, 6, …, n; r=b/a; k(r) and $k_{ij}(r)$ are tabulated shape factors, whose values are shown in Table 1.

Table 1: Coefficients of the polynomial solution for a rectangular fully clamped diaphragm.

r	1	2	3
k(r)	0.02019	0.01035	0.00469
k00	1	1	1
k20	0.233	0.01837	0.00510
k02	0.233	1.27	1.82
k22	0.252	0.195	-0.183
k40	-0.00166	-0.00253	-0.00033
k04	-0.00166	0.475	3.030
k42	0.13	0.00181	0.0306
k24	0.13	0.636	1.46
k44	-0.235	0.0495	0.0844

3.3 Results Comparison

A behavioural model for circular and square diaphragms has been developed based on the previously-mentioned analytical expressions. Both sensors have been designed to present identical capacitance for zero pressure difference between the sealed cavity and the environment surrounding the device.

The sensors are based on PolyMUMPs technology provided by MEMSCAP. The diaphragm is made of polysilicon (Young Elasticity Modulus: E=169GPa; Poisson's ratio: υ=0.22) with a thickness of 4µm, and a 2µm gap between the plates, filled with air sealed at ambient pressure. The circular sensor presents a radius of 350µm, while the square-shaped sensor has a side length of 620.35µm. Pressures up to 60mmHg have been simulated, corresponding to conditions of moderate stenosis.
These two sensors have been modelled in Ansys®. In this way, it is possible to compare results from analytical and FEA simulations, as shown in Fig. 4. It can be noticed that in the case of a square sensor, the error induced by the analytical formulation is proportional to the pressure. This is explained considering the numerical approximation used to
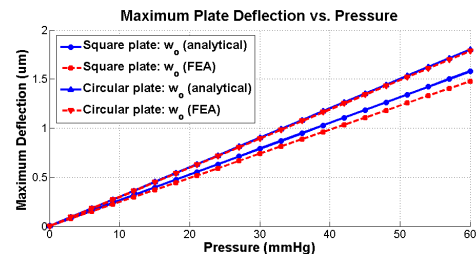

Figure 4: Analytical vs. FEA centre deflection response for circular and square-shaped diaphragms.

solve the differential equation in (4), so a certain deviation is inevitable. Other numerical methods can be used to enhance the accuracy of the model, at the expense of higher complexity and computing times.

4 FE FAULT INJECTION

A complete library of accurate fault models, based on real defects, needs to be developed to enable fault simulations with a realistic estimation of the fault coverage of the test method. The use of FE tools is proposed to analyse the influence of defects occurring during the fabrication or the lifetime of the sensor. The detection and description of defects that give rise to faults will ease the generation of an electrical-compatible behavioural model where new test methodologies could be evaluated.

In this case, FE models of fully-clamped circular and square diaphragms have been built in Ansys®. Defects with different sizes and locations have been inserted on the top plate, where a uniformly distributed pressure is applied. For each particular fault, the capacitance and centre deflection are measured, enabling the evaluation of their influence.

Pyramids grown during the anisotropic wet etching process have been chosen as the case under study. Fig. 5a and Fig. 5b show the capacitance results for circular and square sensors respectively, with pyramids of base areas up to 2500 μm^2 located at the centre of their diaphragms. As expected, the influence of a pyramid is proportional to its size, with bigger pyramids compromising the reliability of the sensor due to strong sensitivity losses. It can be noticed that the sensitivity loss is higher for circular plates (8.77% loss for a 50x50μm^2 pyramid) than for their square counterparts (4.8% loss). In Fig 6a and Fig. 6b the capacitance results for both sensors, under the influence of a pyramid of 50μm base side placed at different locations, are shown. In a fault-free case, the centre and anchoring locations of a circular plate present the maximum bending conditions. On the other hand, a square diaphragm has its critical stress density spots located at its centre, at its side midpoint (θ=0º) and at the midpoint of the semi-diagonal of the plate (θ=45º). The presence of rigid pyramids at these locations prevents any bending of the plate, reducing the sensitivity of the sensor.

In order to probe the accuracy of the simulation results, several prototype PolyMUMPs capacitive pressure sensors have been designed and fabricated. These sensors have been conceived to be part of an ISR monitoring smart stent device, designed to be
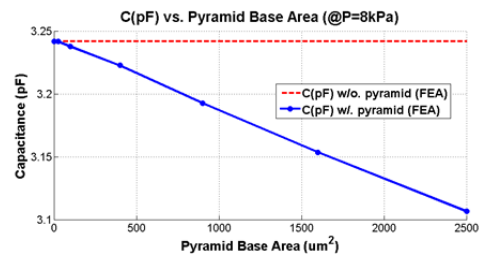

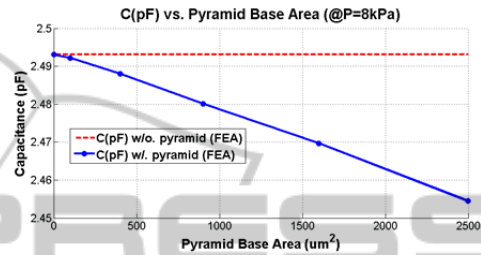Figure 5a: Capacitance vs. pyramid base area: circular sensor.

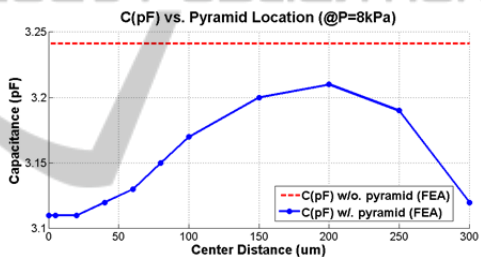Figure 5b: Capacitance vs. pyramid base area: square sensor.

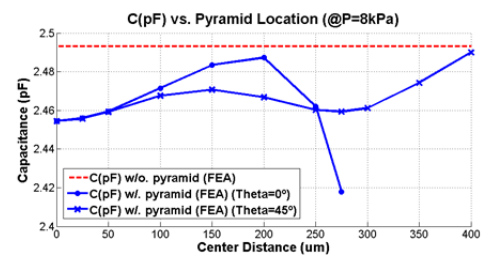Figure 6a: Capacitance vs. pyramid location: circular sensor.

Figure 6b: Capacitance vs. pyramid location: square sensor.

implanted in a distal ramification of the pulmonary artery. Hence, the sensors must be capable of bearing pressure ranges between light (Pmin = 30mmHg) to moderate (Pmax = 60mmHg) stenosis conditions. Both fault-free (Fig. 7) and fault-injected (Fig.8) sensors have been fabricated, and are expected to be measured under in-vitro conditions once coated with the biocompatible materials.
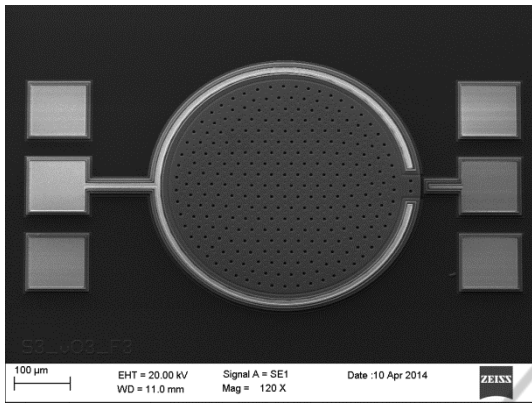
Figure 7: SEM picture of a fault-free PolyMUMPs circular capacitive pressure sensor.
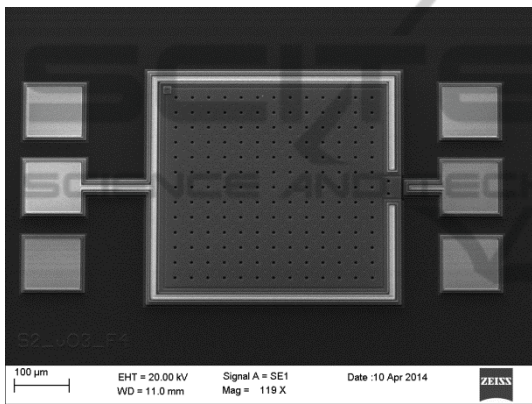

Figure 8: SEM picture of a fault-injected PolyMUMPs square capacitive pressure sensor (injected fault located on the top left corner of the sensor).

5 CONCLUSIONS

In this work, fault modelling problems affecting MEMS capacitive pressure sensors for ISR detection have been analysed. The most common failure mechanisms and defects that generate faulty behaviours have been introduced.

The deflection modelling of circular and rectangular diaphragms has been proven to be solvable via analytical expressions and numerical approximations for the fault-free case. However, these mathematical methods are no longer valid to describe the behaviour of MEMS sensors under certain faulty conditions, where their material properties and geometry are affected. In order to obtain a realistic fault model in all these cases, the use of FE tools is required.

The development of a realistic fault model library, as well as a comprehensive MEMS testing

approach, depends on the methodology extension of to any other faulty conditions detected during MEMS fabrication process and its useful lifetime.

REFERENCES

Nichols M. et al., *Cardiovascular Disease Statistics 2012*, European Heart Network, Brussels. European Society of Cardiology, Sophia Antipolis, 2012.

Garcia Blanco B. et al., Spanish Registry on Cardiac Catheterization and Interventional Cardiology: XXII Official Report of the Working Group on Cardiac Catheterization and Interventional Cardiology of the Spanish Society of Cardiology (1990-2012), *Revista Española de Cardiología*, vol. 66, pp. 894-904, 2013.

Wolff T. et al., Screening for carotid artery stenosis: an update of the evidence for the US Preventive Services Task Force, *Annals Internal Medicine*, vol. 147, pp.854-859, 2007.

Fowkes F.G. et al., Comparison of Global Estimates of Prevalence and risk factors for peripheral artery disease in 2000 and 2010: a systematic review and analysis, *Lancet*, vol. 382, pp. 1329-1340, 2013.

Tendera M. et al., ESC Guidelines on the diagnosis and treatment of peripheral artery diseases. Document covering atherosclerotic disease of extracranial carotid and vertebral, mesenteri, renal, upper and lower extremity arteries: the Task Force on the Diagnosis and Treatment of Peripheral Artery Diseases of the European Society of Cardiology (ESC), *European Heart Journal*, vol. 32, pp. 2851-906, 2011.

Rosing R., Reichenbach R., Richardson A., Generation of component level fault models for MEMS, *Microelectronics Journal*, vol. 33, pp. 861-868, 2002.

Landsberger L. M., Nashed S., Kahrizi M., Paranjape M., On Hillocks Generated During Anisotropic Etching of Si in TMAH, *Journal of Microelectromechanical Systems*, vol. 5, no. 2, pp. 106-116, 1996.

Takahata K., Gianchandani Y. B., Wise K.D., Micromachined antenna stents and cuffs for monitoring intraluminal pressure and flow, *Journal of Microelectromechanical Systems*, vol 15(5), pp. 1289-1298, October 2006.

Timoshenko S., Woinowsky-Krieger S., *Theory of Plates and Shells*, McGraw-Hill, New York, 1959.